Title

Dislocation generation in diamond under extreme loading

Permalink

https://escholarship.org/uc/item/3641n5tm

Authors

Li, Alex C

Li, Boya

Rudd, Robert E

et al.

Peer reviewed

Article

Dislocation generation in diamond under extreme loading

Dislocation Generation in Diamond under Extreme Loading

Diamond is an important material for a variety of applications and, principally, for the capsules holding fusion fuel in National Ignition Facility experiments. By better understanding the evolution of defects and plasticity in diamond, we hope to improve our models and capsule design for nuclear fusion as an energy source.
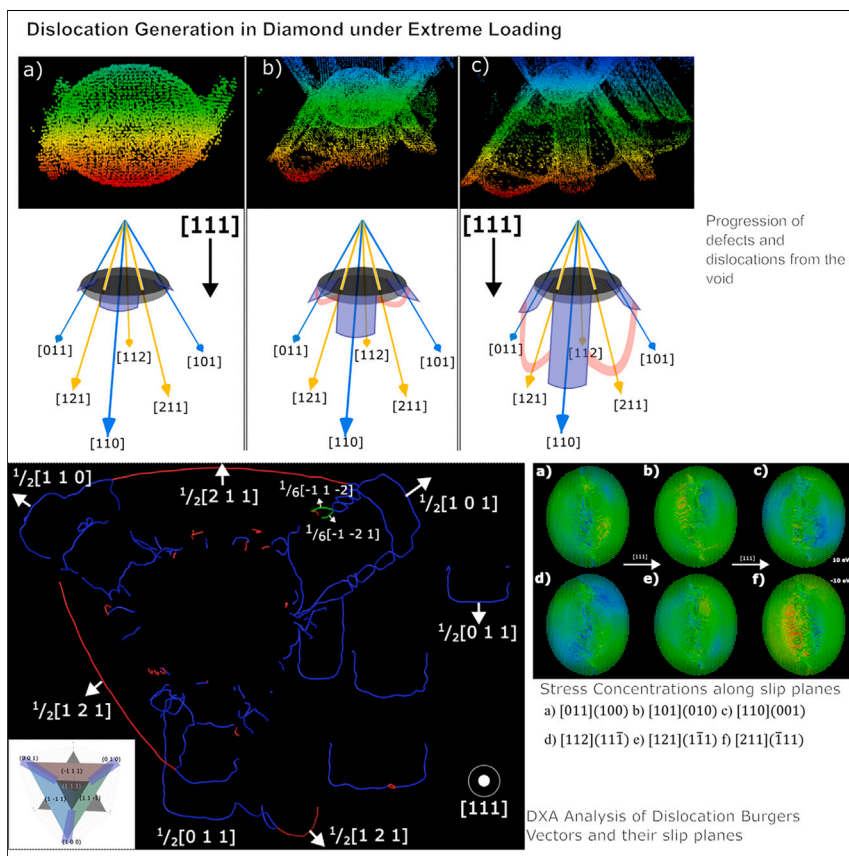
Alex C. Li, Boya Li, Robert E. Rudd, Marc A. Meyers

mameyers@ucsd.edu

Highlights

Strong orientation dependence found in the evolution of plasticity in diamond

Unusual [110](001) and $[112](11\bar{1})$ defects were produced from shock compressed voids

Collapsing voids generate shear stresses along slip planes over triple the bulk stress

Resolved shear-stress analysis may explain defect presence along specific slip systems

2

Benchmark
First qualification/assessment of material properties and/or performance

Matter

CellPress

Article

Dislocation generation in diamond under extreme loading

Alex C. Li,[1] Boya Li,[1] Robert E. Rudd,[2] and Marc A. Meyers[1,3,*]

SUMMARY

Diamond is, by virtue of its high bonding forces and Peierls-Nabarro barrier stresses, among the hardest materials on earth due to the difficulty of generating and moving dislocations. We demonstrate, using molecular dynamics and analytical calculations, that the generation of defects is dependent on loading orientation. Shock-loading single-crystal diamond along [001] and [011] to a stress of 137 GPa did not reveal dislocations, whereas loading along [111] generated profuse dislocations. The introduction of a void at the latter orientation generated dislocations at 72.6 GPa. Two slip systems were identified: <011>{100} and <112>{111}. The threshold for plastic deformation in diamond is orientation dependent and significantly lower than reported in previous studies: 0.14 G (shear modulus). The void collapse generated localized amorphization for [001]. These results on the anisotropy of plasticity and void effects have relevance for the improvement of symmetry in the collapse of diamond capsules in inertial fusion experiments.

INTRODUCTION

Diamond carbon is one of nature's strongest naturally occurring materials. Despite the low atomic packing factor for diamond-cubic systems, the immense strength of the carbon-carbon bonds and the related limitations on dislocations gives diamond extreme hardness and stiffness.[1,2] It is a material of great interest in many applications, including the evolving understanding of carbon-rich exoplanets,[3–5] as well as in the material for the fuel-holding capsules used in recent National Ignition Facility (NIF) inertial confinement fusion experiments.[6–8] It is well known, by virtue of its covalent bonding, that the bonds of diamond are highly directional.[9] This results in difficulty in the generation and mobility of dislocations within its crystalline lattice. Moreover, diamond also exhibits strong anisotropic behavior depending on the direction of applied stress.[10–12] In many shock-compression experiments, diamond has shown little to no plastic behavior until reaching extreme conditions for both pressure and temperature.[10,13,14]

Understanding the response of diamond under shock is particularly important for its role in the current inertial confinement fusion effort. The diamond capsules used in these experiments hold the tritium and deuterium fuel and act as ablative material to produce the extremely high pressures and temperatures needed to initiate fusion. Porosity or other imperfections in the diamond can generate instabilities within the inertial confinement process, leading to imperfect compression and a failure to reach the critical conditions required for fusion.[15] By better understanding diamond's behavior under shock, the instabilities and their disastrous effects could be eliminated.

PROGRESS AND POTENTIAL

Diamond carbon is an important material in many aspects of science and industry but particularly in the efforts of high-energy laser systems such as the National Ignition Facility at Lawrence Livermore National Labs. It is used as an ablative and capsule material for producing the extremely high pressures needed to cause nuclear fusion reactions that are being investigated intensively as a source of energy. Defects present within the diamond capsules that hold the fusion fuel can cause imperfect compression, resulting in a failure to ignite. Here, we study the evolution of plasticity in diamond along different loading orientations and the effects that voids within the material can have on stresses within the diamond. With a better understanding of anisotropy of plasticity, we can create better models or better capsules to get closer to realizing fusion as an energy source.

Table 1. Loading orientations, piston velocities, global pressure, and shock/transverse/shear stresses (GPa) for the simulations presented in this paper

Loading orientation	Piston velocity (km/s)	Global pressure (GPa)	σ_{33}	σ_{11}	σ_{22}	τ_{max}	τ_l
[001]	3.5	137	267	72.3	72.3	97.6	196
[011]	3.5	123	272	83.1	14.3	129	260
[111]	2.0	54.2	145	9.49	8.05	68.6	133
[111]	2.5	72.6	188	15.8	13.5	87.5	171
[111]	3.0	91.4	226	25.6	23.0	101	198
[111]	3.5	119	266	50.3	40.2	113	223

A study of compression of diamond nanopillars with *in situ* transmission electron microscopy (TEM) found a lack of activity when compressed in the [100] direction but profuse dislocation generation in the [110] and [111] directions.[12] The compression of diamond nanospheres also gives evidence of the effects of nanostructure morphology on defect generation.[16] It is well known that voids can act as stress concentrators, lowering the critical stress necessary for the development of dislocations and defects in materials,[17–19] and that small-grained industrial diamond is commonly under-dense.

The molecular dynamics (MD) study supplemented by analytical calculations reported here had as primary objective the characterization of defects introduced by high-strain-rate compressive shock stresses. When shock-wave compression produces extremely high strain in uniaxial strain, more conventional modes of deformation or failure can be suppressed. This is the regime experienced by capsules in the NIF experiments and by diamond in other ablation experiments. The uniaxial strain state also produces alternative stress states compared to classic uniaxial stress compression, which can alter the types of dislocations generated within the material. To generate defects in this study, the applied loading direction was varied; voids were also introduced in order to increase the local shear stresses in an effort to propitiate conditions for defect generation in diamond-like carbon. Indeed, the voids often occur in experiments and can affect the symmetry of capsule collapse.

RESULTS AND DISCUSSION

We performed MD simulations on three orientations of diamond under shock compression. Hereafter, "diamond" refers to carbon in the diamond-cubic structure. It has been shown[12,20] that diamond has a strong anisotropic behavior, and this stimulated our exploration of the three loading directions [001], [110], and [111]. Shock compression was applied because this is the regime experienced during impact events. Shock compression generates a state of uniaxial strain, in contrast with conventional compression loading, which generates a state of uniaxial stress. The piston velocities, shock pressures, and stresses imposed are provided in Table 1.

Shear stresses generated in shock compression

The maximum shear stress for uniaxial strain compression along the x_3 direction is[17,18]

$$\tau_{max} = \frac{|\sigma_3 - \sigma_1|}{2}, \qquad \text{(Equation 1)}$$

where σ_3 and σ_1 are the largest and smallest principal stresses, respectively. For the case of stress localization at the surface of a void, using the equation for a spherical inclusion[21] the maximum local shear stress (τ_l) is

[1]Program of Materials Science and Engineering, University of California, San Diego, La Jolla, CA 92093, USA

[2]Materials Science Division, Lawrence Livermore National Laboratory, Livermore, CA 94550, USA

[3]Lead contact

*Correspondence: mameyers@ucsd.edu

https://doi.org/10.1016/j.matt.2023.06.044

Matter
Article

CellPress

$$\tau_l = \left[1 + \frac{13 - 5\nu}{2(7 - 5\nu)}\right]\tau_{\max}, \qquad \text{(Equation 2)}$$

where the Poisson ratio ν for uniaxial strain, defined as the ratio of lateral ($\varepsilon_{11} = \varepsilon_{22}$) and longitudinal strain (ε_{33}) can be written as

$$\nu = \frac{\sigma_{11}}{\sigma_{33} + \sigma_{11}} \qquad \text{(Equation 3)}$$

because, under uniaxial strain,

$$\varepsilon_{11} = \varepsilon_{22} = 0 = \frac{1}{E}[\sigma_{11} - \nu(\sigma_{33} + \sigma_{22})] = \frac{1}{E}[\sigma_{22} - \nu(\sigma_{33} + \sigma_{11})]. \qquad \text{(Equation 4)}$$

Previous work has shown that the addition of voids can aid in defect generation, including dislocations. This effect is due to the fact that the presence of a void increases the shear stresses in selected places on the surface. The normal stress at the void surface is zero (traction free), generating maximal shear stresses at 45° to it. This was quantified by Traiviratana et al.,[22] Bringa et al.,[23] and Flanagan et al.,[18,19] among others.[24–29] Thus, a 4-nm (diameter) void was introduced in our simulations in order to increase the local stresses within our simulation and stimulate the generation of defects in diamond.

Simulations of shock compression in [001] oriented diamond

For the case of a piston driving the [001] sample at 3.5 km/s, the total pressure (P) within the system reached 137 GPa, with a shock stress (σ_{33}) of 267.4 GPa in the direction of loading (x_3) and 72.26 GPa in the transverse directions (σ_{11}, σ_{22}). Applying Equation 1, a maximum bulk (global) shear stress ($\tau_{\max}$) of 97.5 GPa is obtained. The Poisson's ratio $\nu = 0.2132$ is obtained from Equations 2 and 3; thus, $\tau_l = 195.5$ GPa, or almost exactly a factor of two higher than the maximum bulk shear stress.

In the [001] direction, little to no dislocation activity is observed (Figure 1A). The diamond structure identification algorithm in OVITO[30] shows that some areas of elastic compression change local coordination by amounts enough to register as only first- or second-nearest-neighbor crystalline diamond, but no defects or dislocations are formed or propagated. For the {001} slip systems observed by Nie et al. for diamond,[12] the resolved shear stress for the [001] loading direction is zero. It will be shown in the analysis section that the resolved shear stress for {100} slip is zero. Highly unusual for a cubic crystal, this characteristic helps explain the lack of defect generation. The introduction of a void did not generate dislocations in this orientation. Only some amorphization of material was observed, an irreversible transformation due to the extreme deformation involved in the collapsing void (Figure 1B). This lack of defect generation for shock in the [001] direction of diamond is supported by TEM results taken for diamond shocked up to 40 GPa in pulsed laser shock-compression experiments (Figure 2). Experimental details are provided in the methods section.

Simulations of shock compression in [111] oriented diamond

Simulations performed on diamond with the shock propagation direction oriented along its [111] axis yielded defects at pressures where little to no activity was observed for the [001] shock propagation direction. In the absence of a void, planar defects emerged from the piston impact surface creating dislocations in the {100} planes with ½<110> Burgers vectors. As these dislocations advance, they leave planar stacking faults in their wake, with a constant width bounded by a screw-character dislocation with the same Burgers vector (Figure 3).
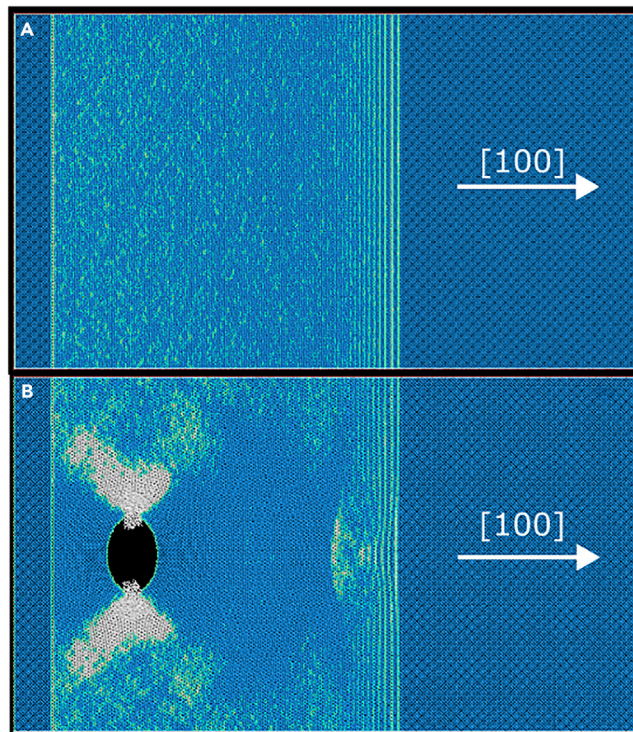
Figure 1. 137 GPa simulation (3.5 km/s piston velocity) for [001] shock-loading direction
Blue color indicates perfectly matched diamond structure, green indicates first or second nearest-neighbor diamond cubic, and white indicates a non-diamond structure.
(A) In the absence of a void, no dislocations or non-diamond regions can be seen under these shock-loading conditions.
(B) With a void, there is a region of crystallinity that OVITO does not recognize as diamond cubic but is simply compressed beyond the ability for the algorithm to categorize it as such. No lasting dislocations or defects form from the void, although some material jetted into the void.

The maximum pressure within the system for the [111] oriented shock propagation direction at a pressure (piston velocity of 3.5 km/s) is 118 GPa, with corresponding values of σ_{11} = 50.3 GPa, σ_{22} = 40.2 GPa, and σ_{33} = 266.0 GPa. Applying Equations 1, 2, and 3, a maximum shear stress of τ_{sg} = 129.1 GPa and τ_{sl} = 302.0 GPa is obtained. Thus, the presence of the void significantly increases the shear stresses.

In the presence of a void, similar ½<011>{100} defects are generated at three points symmetrically around the void, corresponding to the {100} planes. The initial formation of these dislocations from the void can be seen in Figure 4. Two views are imaged: facing the [111] direction (Figure 4A) and from the side [01$\bar{1}$] direction (Figure 4B). These are perfect dislocations on {100} planes with ½<011> directions. Five of the six systems activate dislocations. The dislocations emanating from the void surface relax the elastic shear stresses in the region, and thus some systems are inhibited from growing. There is competition among the dislocations, and some advance faster than the others. This is seen all the way to their full development. Two of these move toward the front and three away from it. As the shock progresses, these initial defects are joined by half loops with ½<112>{111} Burgers vectors (Figure 5). These ½<112>{111} half loops are consistent with the sum of the two ½<011> Burgers vectors that they connect. Thus, {111} is also a slip plane, with a Burgers vector ½<112>{111}. ½<112>{111} seems to be a new superdislocation that has formed as a result of the interaction between the void and the ½<011>{100} dislocations emanating

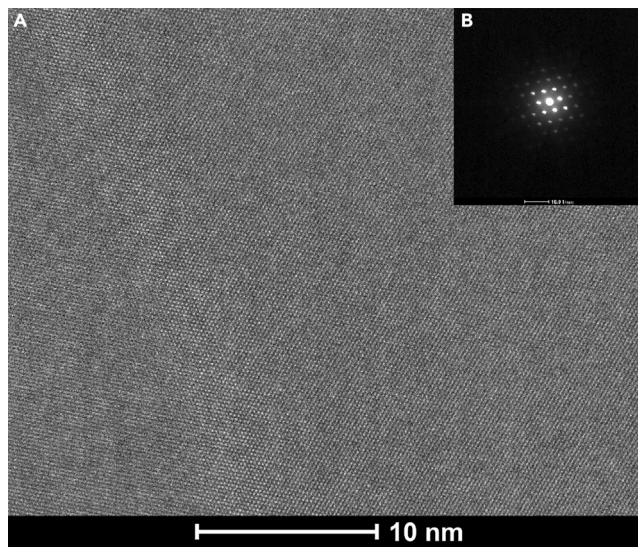# Matter
Article

CellPress

Figure 2. TEM image of preserved crystallinity in [001] oriented diamond shocked to approximately 40 GPa
(A) The crystalline order of the system is perfectly preserved, with no evidence of any plastic deformation.
(B) Diffraction pattern of the area indicating perfect crystalline order.

from it. A visualization of the shear-stress magnitudes resolved on these different slip systems is provided in Figure 6. The per-atom virial stresses were rotated onto the relevant slip planes, and when comparing the averages of the maximum 100 atomic shear stresses at the void surface with the τ_{max} the stresses around the void were found to be between 1.6 and 3.4 times higher, as seen in Table 2. This stress concentration matches our expected stress concentration for an ideal spherical void, and the higher stress concentrations could come from the void's collapse, which changes its shape from spherical to a prolate ellipsoid, thus increasing the stress concentration.

Interestingly, Pirouz et al.,[31] in a systematic TEM study of diamond deformed at 1,800°C, observed the formation of dislocations on {111} planes. The ½<110>{111} dislocations decomposed into partials with a separation of ~4 nm, from which the stacking-fault energy could be calculated. The 3-fold symmetry of these stacking faults and half loops is reminiscent of the results obtained by Nie et al.[12] in their nanopillar experiments, with the rectangular stacking faults consistent in plane and direction with the {100} half loops that they found. However, the presence of the ½<112>{111} dislocation is a new feature in this shock-compression MD study. The dislocation analysis (DXA) of the defects within the simulation was performed in OVITO to determine the location and Burgers vector of these dislocations (Figure 7).

Exploring further, [111] simulations were performed at several different piston velocities to obtain information on the threshold of dislocation generation with and without voids. The 2.0 km/s piston velocity generates a maximum total pressure of 54.2 GPa with maximum bulk shear and local shear stresses of τ_{sg} = 68.6 GPa and τ_{sl} = 133.4 GPa, respectively. At 2.5 km/s the maximum total pressure is 72.6 GPa, with maximum bulk and local shear stresses of τ_{max} = 87.5 GPa and τ_l = 170.6 GPa, respectively. At 3.0 km/s the maximum total pressure is 92.4 GPa, with maximum bulk and local shear stresses of τ_{max} = 101.3 GPa and τ_l = 198.4 GPa, respectively.

At 52.4 GPa (2.0 km/s piston velocity), and in the absence of a void, no defects are generated at the planar impact surface (Figure 8A). When a void is introduced, the
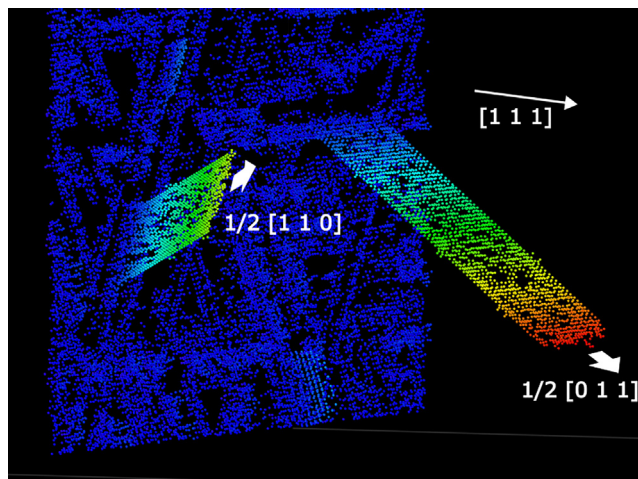
Figure 3. Simulation of [111] compressed diamond at 91.4 GPa (2.5 km/s piston velocity) 5 ps into the simulation

Two distinct defects can be seen emanating from the piston surface. The orientations of these faults are in the {100} family of planes in the <110> directions.

onset of ½<110>{100} dislocations can be seen emerging from the compressed void (Figure 8B). From this emission it is concluded that the presence of a void or other defect-generation site can significantly lower the threshold for dislocation activity and the beginning of plasticity within diamond, depending on its orientation. This effect has been previously analyzed and quantified by Traiviratana et al.,[22] Bringa et al.,[23] and Flanagan et al.[18,19] for other materials and is a direct consequence of the increased maximum shear stress generated by the presence of a void. The threshold stress is also dependent on void size, as has been demonstrated.[17] This dependence is due to the image forces produced by the free surface of the void, proportional to the curvature (inverse of radius). As the pressure is increased to 72.6 GPa (piston velocity of 2.5 km/s), the defect generation from both the planar impact surface and the compressed void increase rapidly. At 91.4 GPa (3.0 km/s), defect generation was even more pronounced.

Measurements of the elastic wave and defect propagation velocities indicate that the defects within the simulations approach the shear-wave velocity limit of diamond (Figure 9) without exceeding it. Shear-wave velocities were calculated directly from the Tersoff potential as $\sqrt{\frac{G}{\rho}}$, where G is the relevant shear modulus for the shear-wave direction and polarization and ρ is the density in the compressed state. For the three orientations of interest, G is C_{44} for <001> (both polarizations), C' and C_{44} for <110>, and C_{111} for <111> (both polarizations). Here, $C' = (½)(C_{11} - C_{12})$ and $C_{111} = (2C' + C_{44})/3$. The wave velocities compare favorably with those taken from the literature.[32] As the pressure is increased the dislocation velocity also increases, without reaching the shear-wave velocity. This is in line with the expected relativistic behavior of fast dislocations, whose energy increases with velocity. Partial dislocations, on the other hand, are known to sporadically exceed the shear-wave velocity, but only for picoseconds,[33,34] and transonic dislocations have been observed in special cases in MD simulation but not yet in experiments.[35]

Simulations of shock compression in [011] oriented diamond

When simulating [011] oriented diamond without a void, no plasticity was observed, as in the [001] oriented diamond. No defects formed from the piston surface or within the bulk simulation at a pressure of 123 GPa (piston velocity 3.5 km/s), with
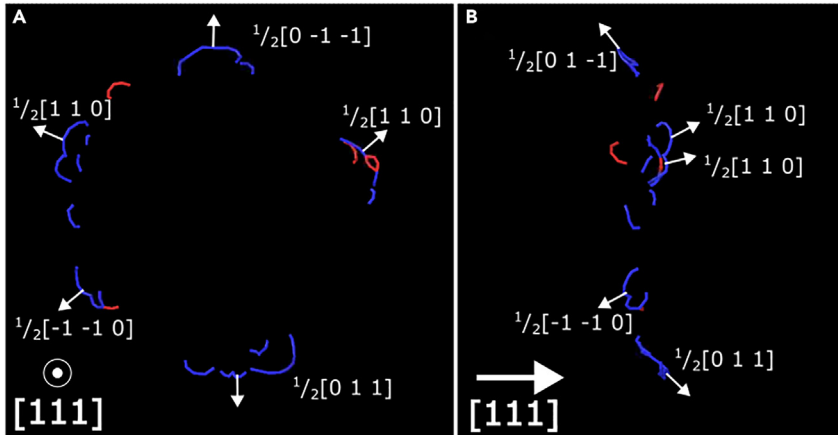
⌬ CellPress

Figure 4. Initiation of defects from the void
Image captured using DXA analysis at 1.5ps in the [111] loading orientation, just as the shock wave has finished passing over the void and the defects have initiated. Several defects can be seen to initiate opposite to the direction of shock. Blue dislocation lines indicate dislocations that lie in the {100} planes. Red dislocation lines are in various other slip systems.
(A) Viewed facing the [111] direction, with shock direction out of the page.
(B) Viewed from the side [01$\bar{1}$] direction, with shock direction to the right.

values of $\sigma_{11} = 83.1$ GPa, $\sigma_{22} = 14.3$ GPa, and $\sigma_{33} = 272$ GPa. However, the presence of a void triggers the formation of a dislocation loop in the ½<112>{111} system but lacks the ½<110>{001} dislocations that might have been expected to form (Figure 10). There is still significantly more dislocation activity present than in the [001] case, and the presence of large <112> oriented defects may be explained by the large resolved shear stress for the [211]($\bar{1}$11) slip system. While there was a high population of non-diamond atoms within the [011] oriented system, the DXA algorithm was not as able to conclusively identify the presence of large and sustained dislocation loops as observed in the [111] oriented system.

Analysis: Calculation of resolved shear stresses on the slip systems

The generation and motion of dislocations is driven by the shear stresses applied to the slip systems. The direction of maximum shear forms a cone 45° away from the direction of shock propagation, and the slip systems most closely aligned with this maximum shear experience the highest resolved shear stress.[36] These calculations have traditionally been done using the Schmid factor and, in the simplified case, assuming isotropy in the elastic properties of materials. We conduct here a more rigorous analysis that accounts for the uniaxial strain state produced by shock compression and the anisotropy of the elastic stiffness matrix of diamond. When transforming the stiffness tensor to the [111] orientation and applying a condition of [111] uniaxial strain, values are obtained for all six components of the stress within the system. A similar procedure is followed for the [001] orientation. The presence of these shear stresses drives the three-dimensionality of the defects and dislocations observed in our diamond simulations. This is presented below.

Dislocation generation and motion is driven by shear stresses. The general form of the resolved shear stress on a slip plane is given as

$$\sigma_{1'2'} = \sigma_{11}l_{1'1}l_{2'1} + \sigma_{22}l_{1'2}l_{2'2} + \sigma_{33}l_{1'3}l_{2'3}$$
$$+ \sigma_{12}(l_{1'1}l_{2'2} + l_{1'2}l_{2'1}) + \sigma_{23}(l_{1'2}l_{2'3} + l_{1'3}l_{2'2}) + \sigma_{13}(l_{1'3}l_{2'1} + l_{1'1}l_{2'3}).$$

(Equation 5)

The cosine matrix l_{ij} is used, where the values are defined as the direction cosines of the loading coordinate system and the coordinate system is defined by the slip
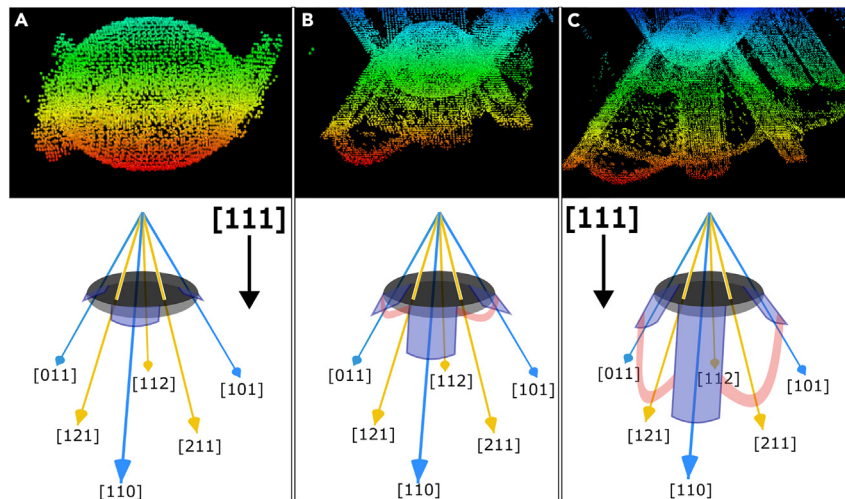
Figure 5. Evolution of the defects emanating from the void for [111] loading orientation
The 3-fold symmetric straight bands are the same as the bands seen in the case without a void present, <110> direction in the {100} plane. In addition, loops with Burgers vector ½<112> appear on the {111} planes between these three straight bands. While the straight <110> defects leave behind a stacking fault, the <112> dislocations do not. (A) 1 ps; (B) 2.5 ps; (C) 4 ps.

direction, slip plane normal, and normal to slip direction in the slip plane. The angles between directions are calculated by the scalar product of vectors. The rotation matrix is

$$l_{ij} = \cos\left(\overrightarrow{e_i}', \overrightarrow{e_j}\right) = \begin{bmatrix} l_{1'1} & l_{1'2} & l_{1'3} \\ l_{2'1} & l_{2'2} & l_{2'3} \\ l_{3'1} & l_{3'2} & l_{3'3} \end{bmatrix} \qquad \text{Equation 6}$$

where $\overrightarrow{e_i}'$ is the new rotated coordinate system and $\overrightarrow{e_j}$ is the old coordinate system.

For a state of uniaxial stress, the resolved shear stress (τ_r) on the slip plane and slip direction is calculated through the well-known Schmid factor (m):

$$\tau_r = m\sigma_{33}, \qquad \text{(Equation 7)}$$

$$m = \cos(\lambda)\cos(\varphi), \qquad \text{(Equation 8)}$$

where λ and φ are the angles between the loading direction and the vector along the slip direction and the vector normal to the slip plane, respectively. For the Schmid factor, $\cos(\lambda)$ and $\cos(\varphi)$ correspond to $l_{1'3}$ and $l_{2'3}$, respectively. Because in this case there are no lateral stresses present, all stress terms other than σ_{33} are zero. In terms of the generalized indicial notation, the shear stress is expressed as

$$\sigma_{1'2'} = \sigma_{33} l_{1'3} l_{2'3} . \qquad \text{(Equation 9)}$$

While the Schmid factor describes a state of uniaxial stress, for a uniaxial strain state generated by shock compression, lateral expansion is constrained. Thus, in addition to the shock stress generated by the piston, lateral compressive stresses are generated, which have to be computed in the calculation of the resolved shear stresses. Figure 11 shows a unit cube subjected to tridimensional compression and the relationship of the slip system (plane and direction) with the cube coordinate axes, which have the x_3 direction aligned with the shock propagation direction. This is done here, following the procedure developed by Lu in her doctoral dissertation. The first step is to obtain the stiffness matrix for the three orientations by applying a rotation of the stiffness tensor. The elastic stiffness (C'_{ijkl}) transformation equation is
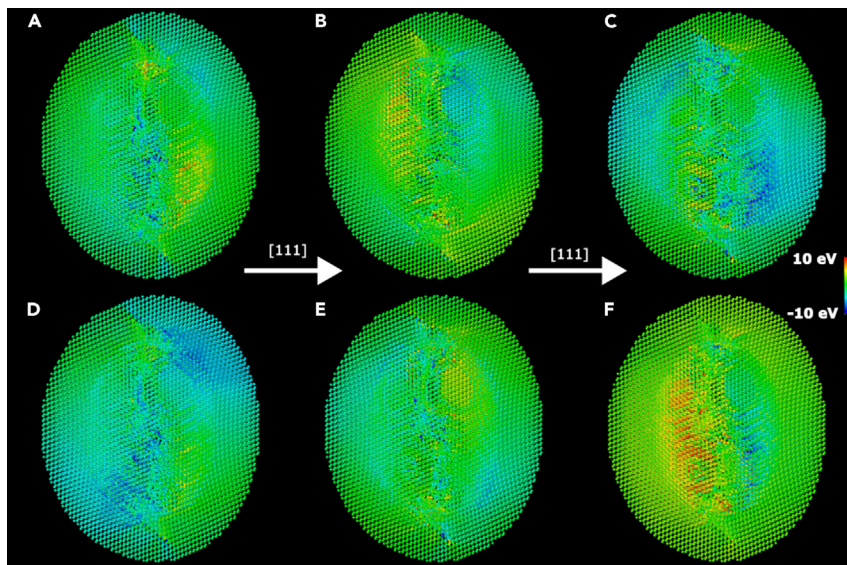
CellPress

Figure 6. Resolved shear stresses along different slip systems
A sphere was formed around the void with a 6 nm radius, and per-atom stress values were taken after the shock wave had passed through the void and dislocations just began to form. The different resolved shear stresses show the directional differences in the stress concentrations for the different slip systems, which may result in the formation of dislocations. The color scale on the right indicates the magnitude of the stress being experienced by the atoms, with red and blue indicating the two extremes. (A) [011](100); (B) [101](010); (C) [110](001); (D) [112](11$\bar{1}$); (E) [121](1$\bar{1}$1); (F) [211]($\bar{1}$11).

$$C'_{ijkl} = l_{im}l_{jn}l_{ko}l_{lp}C_{mnop} . \qquad \text{(Equation 10)}$$

A sum over indices repeated on the right-hand side is implied. Each value in the original stiffness tensor is transformed through four cosine matrix values, then summed together to form one element in the rotated stiffness tensor. The values for the tensors in the [001], [011], and [111] directions are provided in Table 3.

To calculate the stress in the system from the transformed stiffness tensor, we require the true strain within the deformed material, as

$$\sigma = C\varepsilon . \qquad \text{(Equation 11)}$$

The true strain within the shocked material can be obtained from the Rankine-Hugoniot equations for conservation of mass, momentum, and energy as

$$\varepsilon_{33} = \ln\left(\frac{V}{V_0}\right) = \ln\left(1 - \frac{U_P}{U_s}\right) = \ln\left(1 - \frac{U_P}{C_0 + SU_P}\right). \qquad \text{(Equation 12)}$$

Values for C_0 and S for diamond are taken from Hicks et al.,[39] being 11.9 km/ s and 1.01, respectively.

The resulting shear stress can be normalized to the shock stress to provide the Lu factor: $m_{Lu} = \sigma_{1'2'}/\sigma_{33}$ in uniaxial strain. In Table 4 the Schmid and Lu factors are presented for the two families of slip systems: <211>{111} and <110>{001}. The

Table 2. Stress concentration factors for slip systems comparing the stress at the void surface vs. the bulk

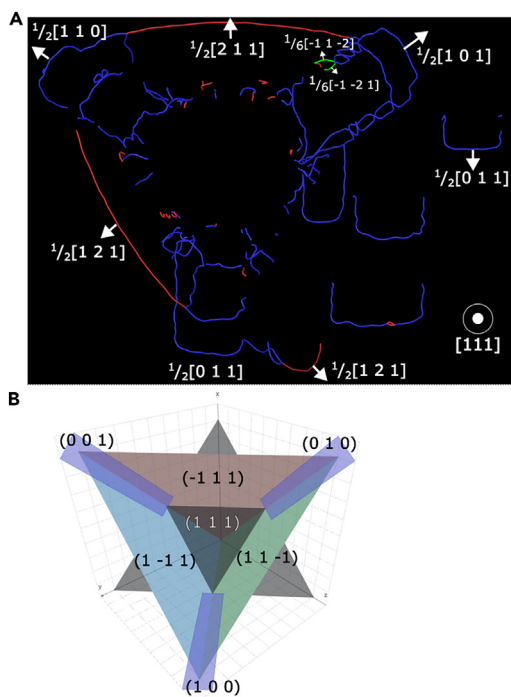| Slip system	[011](100)	[101](010)	[110](001)	[112](11$\bar{1}$)	[121](1$\bar{1}$1)	[211]($\bar{1}$11)
Stress concentration	1.64	3.37	2.89	3.22	2.03	3.16

Figure 7. Dislocations around a void
(A) DXA dislocation and defect analysis of the [111] shocked diamond system at 3.25 ps.
(B) A graphical representation of the planes and orientations of the system. The rectangular bands propagate within the {100} planes, while the half loops connecting them are present along the {111} planes.

Lu factor requires knowledge of the strain and shock stress for normalization; the values for the 3.5 km/s simulations were chosen in each orientation.

Table 4 provides the uniaxial stress (Schmid) and uniaxial strain (Lu) factors for the three shock propagation orientations. The Schmid factor is a simple ratio of the stress on the associated slip system with respect to the applied loading direction under the condition of uniaxial stress, a common loading condition in practice and analysis. The Lu factor is similar, giving the same ratio of stress on the slip system to the shock stress but with the uniaxial loading condition appropriate to bulk shocked materials. In the case of uniaxial strain, the system experiences transverse stresses that do not relax, since the transverse strain remains zero due to inertial
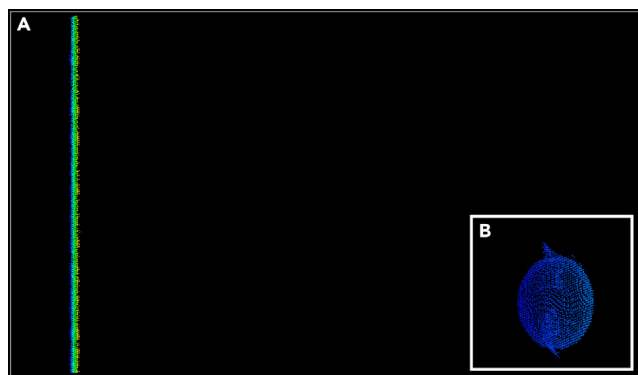

Figure 8. 54 GPa (2 km/s piston velocity) simulation for [111] diamond shock at 10 ps
(A) A view of all atoms within the system with coordination number other than 4, the usual value for diamond. No atoms beyond the piston surface are detected, i.e., all are diamond.
(B) The beginnings of dislocations can be seen to form when a void is present and shocked, but never begin to propagate within the system.
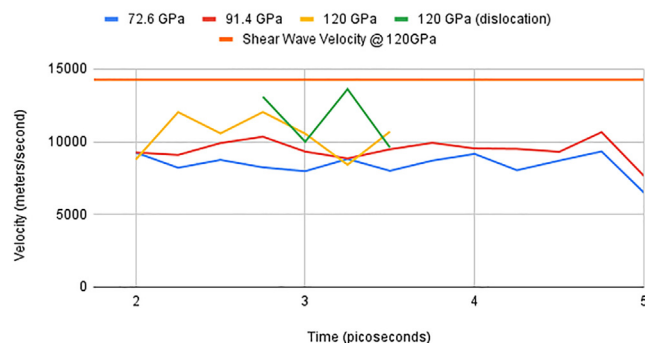
Figure 9. Defect propagation velocity at varying simulation pressures and piston velocities (72.6 GPa = 2.5 km/s, 91.4 GPa = 3 km/s, and 123 GPa = 3.5 km/s)
An additional measurement was made at 120 GPa (3.5 km/s) corresponding to the green line, measuring the propagation velocity of a dislocation. Shear-wave velocity calculated for carbon at 120 GPa using Tersoff potential.

confinement (experiment) or periodic boundary conditions (simulations). These additional stresses lower the shear stress experienced by the slip systems. In the limiting case of hydrostatic loading, where the stress in all directions is equal, there would be no shear stress within the system, whereas the case of uniaxial loading maximizes the shear stress. The condition of uniaxial strain experienced under shock loading lies in between those. For example, in [001] propagation the transverse stress is equal to $(C_{12}/C_{11})\sigma_{33}$, so the stress state is a sum of the uniaxial stress $[1 - (C_{12}/C_{11})]\sigma_{33}$ and a hydrostatic pressure. By the same rationale as explained above, multiplying by the Schmid factor gives the resolved shear stress, since the resolved shear stress is independent of hydrostatic pressure. Thus, for [001] uniaxial strain, the Lu factor is $m_{Lu} = [1 - (C_{12}/C_{11})]m$. In general, the Lu factors within Table 4 are lower in magnitude compared with the Schmid factors, meaning that the slip systems in shock loading experience less shear stress due to the different loading conditions.
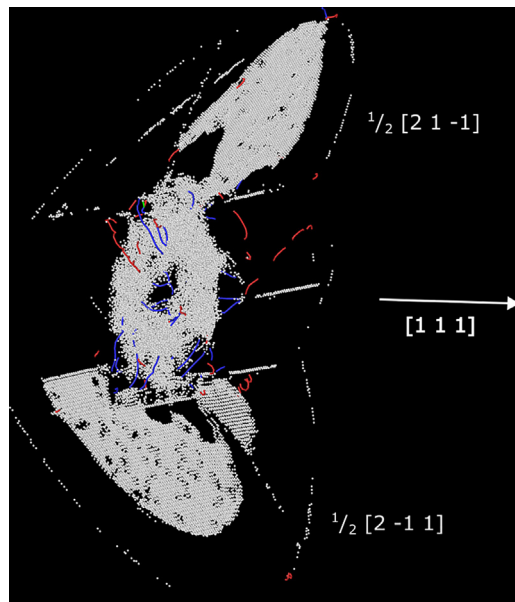

Figure 10. Non-diamond atoms and DXA analysis for [011] shocked diamond at 2.5 ps
The defect bands emanating from the void are oriented in the ½<112> directions and are semicircular in shape as they expand away from the void surface.

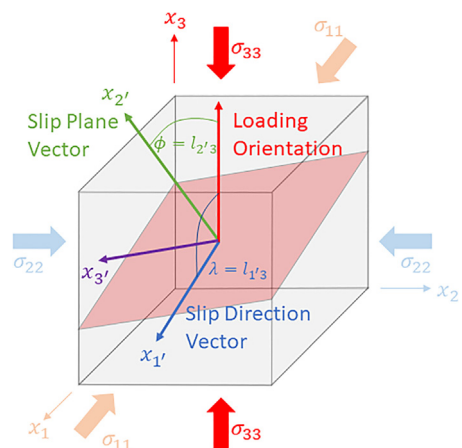**Figure 11. Orientation relationships for shock loading and slip planes**

For the ½<110>{001} dislocations, the relative values for the Schmid factors and Lu factors are quite close. Notably, the value for the [001] loading case are all zero for both the Schmid and Lu factors, which explains the lack of dislocation activity in this loading direction. The [011] loading case has similar results for both as well, with two slip systems having non-zero resolved shear stress. In the [111] direction, all slip systems are active, and this activity is seen in our simulations as well.

For the ½<112>{111} dislocations, the [001] loading direction in fact has non-zero values of resolved shear stress for both the Schmid and Lu factors. However, we still see no dislocation activity along these slip systems for the [001] loading case. These dislocations likely have other conditions necessary for them to form, such as a reaction between two different ½<110>{100} dislocations present in the other systems but not [001]. In the [011] case two of the Schmid factors are zero, but we still have large activity along one slip system. The corresponding Lu factors are non-zero, but the values in the slip systems corresponding to the zero-stress Schmid factors is still apparently too small to generate dislocations. We observe one slip system in the MD simulations for the [011] loading case, matching what is seen in our simulation. For [111] loading, the Schmid factor predicts equal values for each slip system much like for the ½<110>{100} dislocations, and our Lu factors predict the same thing, although with reduced values for the resolved shear stress. However, in our calculation of the resolved shear stress at the void's surface, we found that for the two directions where the half loop is present, the average stress concentration at the void's surface was over 20 times that of the bulk, whereas for the missing direction it was only 3 times that of the bulk. This difference in the stress concentration along the particular orientation could explain why the final half loop was missing.

While MD simulations are helpful tools for understanding materials behavior and exploring atomistic detail, they are not without limitations. All calculations performed in a simulation are dependent upon the accuracy of the interatomic potential being used. The Tersoff potential used in this paper is an empirical potential and has shown good performance in modeling both mechanical properties and dislocations in diamond carbon, but it fails to produce accurate results when under even higher pressure (>150 GPa) or temperature conditions. While density functional theory (DFT) simulations provide the highest accuracy available, they are limited to small numbers of atoms due to their computational complexity. Recently, machine-learning potentials that are trained on DFT data such as the Gaussian approximation potential[40] or the spectral neighbor analysis potential[41] have been developed that

Matter
Article

CellPress

Table 3. Transformed stress tensors at ∼140 GPa with change of basis loading direction

$$C_{[001]} = \begin{bmatrix} 2000 & 500 & 500 & 0 & 0 & 0 \\ 500 & 2000 & 500 & 0 & 0 & 0 \\ 500 & 500 & 2000 & 0 & 0 & 0 \\ 0 & 0 & 0 & 1200 & 0 & 0 \\ 0 & 0 & 0 & 0 & 1200 & 0 \\ 0 & 0 & 0 & 0 & 0 & 1200 \end{bmatrix} \qquad \varepsilon = \begin{bmatrix} 0 \\ 0 \\ \varepsilon_3 \\ 0 \\ 0 \\ 0 \end{bmatrix} \qquad \sigma_3 = \varepsilon_3 \begin{bmatrix} 500 \\ 500 \\ 2000 \\ 0 \\ 0 \\ 0 \end{bmatrix}$$

$$C_{[011]} = \begin{bmatrix} 2000 & 500 & 500 & 0 & 0 & 0 \\ 500 & 1550 & 950 & -300 & 0 & 0 \\ 500 & 950 & 1550 & 300 & 0 & 0 \\ 0 & -300 & 300 & 1050 & 0 & 0 \\ 0 & 0 & 0 & 0 & 1200 & 0 \\ 0 & 0 & 0 & 0 & 0 & 1200 \end{bmatrix} \qquad \varepsilon = \begin{bmatrix} 0 \\ 0 \\ \varepsilon_3 \\ 0 \\ 0 \\ 0 \end{bmatrix} \qquad \sigma_3 = \varepsilon_3 \begin{bmatrix} 500 \\ 950 \\ 1550 \\ 300 \\ 0 \\ 0 \end{bmatrix}$$

$$C_{[111]} = \begin{bmatrix} 1550 & 650 & 800 & 81.6 & -70.7 & 57.7 \\ 650 & 1550 & 800 & -244 & -212 & -173 \\ 800 & 800 & 1400 & 163 & 282 & 115 \\ 81.6 & -244 & 163 & 700 & -115 & -212 \\ -70.7 & -212 & 282 & -115 & 1100 & -81.6 \\ 57.7 & -173 & 115 & -212 & -81.6 & 1150 \end{bmatrix} \qquad \varepsilon = \begin{bmatrix} 0 \\ 0 \\ \varepsilon_3 \\ 0 \\ 0 \\ 0 \end{bmatrix} \qquad \sigma_3 = \varepsilon_3 \begin{bmatrix} 800 \\ 800 \\ 1400 \\ 163 \\ 282 \\ 115 \end{bmatrix}$$

Original values from Orlikowski et al.,[37] Güler and Güler,[32] and González-Cataldo et al.[38]

can simulate higher energy conditions more accurately, but they are still much more costly in terms of computational power required. Another issue with computation power is that because of time constraints on running simulations, larger simulations and longer simulations are both limited. This means that some size effects may be absent as they cannot be captured, and any defects that do not appear within the short time frame of the simulation may be missed. For example, classical MD is a bad choice for modeling diffusion activity, which happens on much longer time scales than what is traditionally modeled in these types of simulations. With more computing power available it will be possible to extend both the size and time of our simulations to capture more of the development of how the material reacts to shock. Real diamond could have larger defects or elemental impurities that cannot be captured here, which could further lower thresholds for dislocation activity. Amorphization within diamond is another topic of interest, whose nucleation and growth may not be able to be captured within the time frame used here. However, as computing technology improves and access to faster systems becomes available, these issues may be addressed, leading to longer and larger simulations with more accurate potentials that could fully capture the response of diamond or any other material.

Conclusions

It is demonstrated that shock compression at pressures in the range of 72.6 GPa can generate dislocations in single-crystal diamond. A significant orientation dependence of defect generation was observed through shock-compression MD simulations. While few if any defects are generated with shock propagation in the [001] direction, significantly more defect activity is observed in the [011] and [111] orientations under the same shock-compression conditions. When a void was introduced into the system, even more defects were generated, including novel ½<112> superdislocations in the [111] oriented system, which formed half loops connecting the 3-fold symmetric ½<110>{001} dislocations formed at the compressed edge of the void. While the ½<110>{001} dislocations have been experimentally observed previously, the influence of voids or similar defect-generation sites may give rise to new dislocation activity such as seen in our simulations and may help us better understand the response of diamond in experiments that may include such voids or defect sites. These results are consistent with TEM observation of quasistatically loaded single crystals with the same orientations by Nie et al.[12]

Table 4. Schmid and Lu factors (resolved shear stress with transformed tensor) for relevant slip systems

Loading direction	[Slip direction] (slip plane)	m Schmid factor (uniaxial stress)	m_{Lu} Lu factor $\frac{\sigma_{1'2'}}{\sigma_{33}}$ (uniaxial strain, 3.5 km/s)
[001]	[011](100)	0	0
[001]	[101](010)	0	0
[001]	[110](001)	0	0
[001]	[112](11$\bar{1}$)	−0.47	−0.339
[001]	[121](1$\bar{1}$1)	0.23	0.169
[001]	[211]($\bar{1}$11)	0.23	0.169
[011]	[011](100)	0	0
[011]	[101](010)	0.35	0.327
[011]	[110](001)	0.35	0.327
[011]	[112](11$\bar{1}$)	0	0.035
[011]	[121](1$\bar{1}$1)	0	0.035
[011]	[211]($\bar{1}$11)	0.47	0.366
[111]	[011](100)	0.47	0.415
[111]	[101](010)	0.47	0.415
[111]	[110](001)	0.47	0.415
[111]	[112](11$\bar{1}$)	0.31	0.277
[111]	[121](1$\bar{1}$1)	0.31	0.277
[111]	[211]($\bar{1}$11)	0.31	0.277

The results presented here are of relevance in predicting the anisotropy of plastic deformation of polycrystalline diamond under compression and are important in the understanding of the asymmetry of collapse of a capsule under hydrostatic compression. Another important aspect of the findings presented here is a more precise characterization of ablator response. Diamond is among the low Z elements, one of the best choices for ablator in pulsed laser energy deposition.[15] Dislocation generation, amorphization, and energy deposition at voids can lead to shear localization. These effects have not been systematically investigated, and the simulations point to an approach that can elucidate the occurrence and effect of these phenomena.

EXPERIMENTAL PROCEDURES

Resource availability

Lead contact
Further information and requests for resources should be directed to and will be fulfilled by the lead contact, Marc Meyers (mameyers@ucsd.edu).

Materials availability
This study did not generate new unique reagents.

Data and code availability
- All data reported in this paper will be shared by the lead contact upon request.
- This paper does not report original code.
- Any additional information required to reanalyze the data reported in this paper is available from the lead contact upon request.

Methods
The large-scale, open-source MD code LAMMPS was employed to perform classical atomistic molecular dynamics simulations.[42] The Tersoff potential[43] was used as the interatomic potential for carbon, having shown good performance in modeling the mechanical properties of diamond up to the pressures used in this paper, as well as

Matter
Article

in modeling dislocations.[16,44,45] All simulations were performed with the shock along the z direction. For the [001] orientation, the default lattice settings for the diamond system were used. For the [011] orientation, the z axis was oriented along [011], the y axis along [01$\bar{1}$], and the x axis along [100]. For the [111] orientation, the z axis was oriented along [111], y axis along [01$\bar{1}$], and x axis along [2$\bar{1}\bar{1}$]. The initial simulation box size was 100 × 100 × 200 lattice parameters in the x, y, and z axes, or approximately 35.6 nm × 35.6 nm × 71.3 nm. The simulations contained approximately 17 million carbon atoms. Periodic boundaries were applied in the x and y dimensions, with a shrink-wrapped boundary for z. A piston was formed of the atoms in the first 10 lattice parameters in the z direction, and atoms in the region between 11 and 13 lattice parameters were removed. For simulations with a void, the void was 4 nm in diameter, centered in x and y, and placed 23 lattice parameters into the bulk to prevent it from interacting with the piston surface. The time step was 0.5 fs to prevent carbon atoms from interacting unphysically when particle velocities became too high. As shown in Table 1, the piston velocity was set to 3.5 km/s for studying the difference in shock-loading orientation. For the [111] case, piston velocities were then varied from 1.5 to 3.5 km/s to observe defect-generation thresholds. All visualization was performed using OVITO.[30] Structure and defect analysis were performed using the Identify Diamond Structure and DXA analysis packages included in OVITO. For measurements of the stress concentration around the void, a spherical region with a 6 nm radius was constructed around the void, with the per-atom virial stresses calculated for every 100 time steps and averaged over these 100 time steps. These virial stresses were then transformed onto the relevant slip systems by projecting each component onto the relevant Burgers and slip plane vectors and compared with the bulk τ_{max} to find the stress concentration.

The Omega Laser Facility of the Laboratory of Laser Energetics at the University of Rochester was used to shock diamonds under extreme loading conditions and recover them for microscopic analysis. The high laser energy of Omega enabled the imposition of the extreme stress- and strain-rate conditions. Our single-crystal diamond cylinders were synthesized by Almax easyLab. Gold and molybdenum capsules and foils were purchased and processed at the University of California, San Diego Campus Research Machine Shop. The specimen capsule and recovery tube were filled with aerogel intended to decelerate and capture the specimen and recovery capsule. The 1 ns square laser pulse at 196.3 J was applied to a polystyrene ablator, which launched a planar shock into the diamond target. The use of impedance-matched metal capsules is essential to the successful recovery of the specimens and their subsequent characterization, since covalently bonded materials are brittle. Focused ion beam (FIB) was used to prepare very thin foils of about 100 nm, then an FEI Scios Dual Beam FIB/scanning electron microscope was used with gallium ion beam for pattern/lamella milling at different voltages and currents. A thin platinum film of about 3 μm was deposited on the area of interest to protect the sample. A Thermo Fisher Talos 200X G2 scanning transmission electron microscope at 200 kV high tension enabled post-shock characterization and identification of the mechanisms of deformation and failure at the nanometer level.

CellPress

REFERENCES

1. Robertson, J. (1992). Properties of diamond-like carbon. Surf. Coat. Technol. *50*, 185–203. https://doi.org/10.1016/0257-8972(92)90001-Q.

2. Eremets, M.I., Trojan, I.A., Gwaze, P., Huth, J., Boehler, R., and Blank, V.D. (2005). The strength of diamond. Appl. Phys. Lett. *87*, 141902. https://doi.org/10.1063/1.2061853.

3. Wilson, H.F., and Militzer, B. (2014). Interior phase transformations and mass–radius relationships of silicon–carbon planets. Astrophys. J. *793*, 34. https://doi.org/10.1088/0004-637X/793/1/34.

4. Madhusudhan, N., Lee, K.K.M., and Mousis, O. (2012). A possible carbon-rich interior in super-Earth 55 Cancri e. Astrophys. J. *759*, L40. https://doi.org/10.1088/2041-8205/759/2/L40.

5. Mashian, N., and Loeb, A. (2016). CEMP stars: possible hosts to carbon planets in the early Universe. Mon. Not. Roy. Astron. Soc. *460*, 2482–2491. https://doi.org/10.1093/mnras/stw1037.

6. Hopkins, L.B., Lepape, S., Divol, L., Pak, A., Dewald, E., Ho, D.D., Meezan, N., Bhandarkar, S., Benedetti, L.R., Bunn, T., et al. (2018). Toward a burning plasma state using diamond ablator inertially confined fusion (ICF) implosions on the National Ignition Facility (NIF). Plasma Phys. Contr. Fusion *61*, 014023. https://doi.org/10.1088/1361-6587/aad97e.

7. Biener, J., Ho, D.D., Wild, C., Woerner, E., Biener, M.M., El-Dasher, B.S., Hicks, D.G., Eggert, J.H., Celliers, P.M., Collins, G.W., et al. (2009). Diamond spheres for inertial confinement fusion. Nucl. Fusion *49*, 112001. https://doi.org/10.1088/0029-5515/49/11/112001.

8. Zylstra, A.B., Hurricane, O.A., Callahan, D.A., Kritcher, A.L., Ralph, J.E., Robey, H.F., Ross, J.S., Young, C.v., Baker, K.L., Casey, D.T., et al. (2022). Burning plasma achieved in inertial fusion. Nature *601*, 542–548. https://doi.org/10.1038/s41586-021-04281-w.

9. Roundy, D., and Cohen, M.L. (2001). Ideal strength of diamond, Si, and Ge. Phys. Rev. B *64*, 212103. https://doi.org/10.1103/PhysRevB.64.212103.

10. Winey, J.M., Knudson, M.D., and Gupta, Y.M. (2020). Shock compression response of diamond single crystals at multimegabar stresses. Phys. Rev. B *101*, 184105. https://doi.org/10.1103/PhysRevB.101.184105.

11. Lang, J.M., Winey, J.M., and Gupta, Y.M. (2018). Strength and deformation of shocked diamond single crystals: Orientation dependence. Phys. Rev. B *97*, 104106. https://doi.org/10.1103/PhysRevB.97.104106.

12. Nie, A., Bu, Y., Huang, J., Shao, Y., Zhang, Y., Hu, W., Liu, J., Wang, Y., Xu, B., et al. (2020). Direct observation of room-temperature dislocation plasticity in diamond. Matter *2*, 1222–1232. https://doi.org/10.1016/J.MATT.2020.02.011.

13. McWilliams, R.S., Eggert, J.H., Hicks, D.G., Bradley, D.K., Celliers, P.M., Spaulding, D.K., Boehly, T.R., Collins, G.W., and Jeanloz, R. (2010). Strength effects in diamond under shock compression from 0.1 to 1 TPa. Phys. Rev. B *81*, 014111. https://doi.org/10.1103/PhysRevB.81.014111.

14. Wu, H., Luo, X., Wen, L., Sun, H., and Chen, C. (2019). Extreme static compression of carbon to terapascal pressures. Carbon N. Y. *144*, 161–170. https://doi.org/10.1016/j.carbon.2018.12.004.

15. Baker, K.L., Thomas, C.A., Landen, O.L., Haan, S., Lindl, J.D., Casey, D.T., Young, C., Nora, R., Hurricane, O.A., Callahan, D.A., et al. (2023). Reaching a burning plasma and ignition using smaller capsules/Hohlraums, higher radiation temperatures, and thicker ablator/ice on the national ignition facility. Phys. Plasmas *30*, 032702. https://doi.org/10.1063/5.0131180.

16. Garcia Vidable, G., Gonzalez, R.I., Valencia, F.J., Amigo, N., Tramontina, D., and Bringa, E.M. (2022). Simulations of plasticity in diamond nanoparticles showing ultrahigh strength. Diam. Relat. Mater. *126*, 109109. https://doi.org/10.1016/j.diamond.2022.109109.

17. Tang, Y., Bringa, E.M., and Meyers, M.A. (2012). Ductile tensile failure in metals through initiation and growth of nanosized voids. Acta Mater. *60*, 4856–4865. https://doi.org/10.1016/j.actamat.2012.05.030.

18. Flanagan, R.M., Meyers, M.A., Valone, S.M., and Fensin, S.J. (2022). Collapse of helium-filled voids in extreme deformation: Dislocation mechanisms. Mater. Sci. Eng. *839*, 142712. https://doi.org/10.1016/j.msea.2022.142712.

19. Flanagan, R.M., Fensin, S.J., and Meyers, M.A. (2022). The role of pre-existing heterogeneities in materials under shock and spall. Appl. Phys. Rev. *9*, 011305. https://doi.org/10.1063/5.0053693.

20. Hu, Z.F., Lv, S.D., Huang, J.F., Zhang, L., Huang, C.T., Li, Y.W., Huang, W.H., Ye, J.P., and Wei, Q. (2018). Anisotropy effects in diamond under nanoindentation. Carbon N Y *38*, 606–611. https://doi.org/10.1016/j.carbon.2018.02.066.

21. Timoshenko, S., and Goodier, J.N. (1951). Theory of Elasticity (McGraw-Hill).

22. Traiviratana, S., Bringa, E.M., Benson, D.J., and Meyers, M.A. (2008). Void growth in metals: Atomistic calculations. Acta Mater. *56*, 3874–3886. https://doi.org/10.1016/j.actamat.2008.03.047.

23. Bringa, E.M., Traiviratana, S., and Meyers, M.A. (2010). Void initiation in fcc metals: Effect of loading orientation and nanocrystalline effects. Acta Mater. *58*, 4458–4477. https://doi.org/10.1016/j.actamat.2010.04.043.

24. Ashby, M.F. (2006). The deformation of plastically non-homogeneous materials. Philos. Mag. *21*, 399–424. https://doi.org/10.1080/14786437008238426.

25. Rice, J.R., and Thomson, R. (2006). Ductile versus brittle behaviour of crystals. Philos. Mag. *29*, 73–97. https://doi.org/10.1080/14786437408213555.

26. Rice, J.R., and Tracey, D.M. (1969). On the ductile enlargement of voids in triaxial stress fields. J. Mech. Phys. Solid. *17*, 201–217. https://doi.org/10.1016/0022-5096(69)90033-7.

27. Needleman, A., Tvergaard, V., and Hutchinson, J.W. (1992). Void growth in plastic solids. In Topics in Fracture and Fatigue, A.S. Argon, ed. (Springer), pp. 145–178. https://doi.org/10.1007/978-1-4612-2934-6_4.

28. Lubarda, V.A., Schneider, M.S., Kalantar, D.H., Remington, B.A., and Meyers, M.A. (2004). Void growth by dislocation emission. Acta Mater. *52*, 1397–1408. https://doi.org/10.1016/j.actamat.2003.11.022.

29. Meyers, M.A., Traiviratana, S., Lubarda, V.A., Benson, D.J., and Bringa, E.M. (2009). The role of dislocations in the growth of nanosized voids in ductile failure of metals. JOM *61*, 35–41. https://doi.org/10.1007/S11837-009-0025-7.

30. Stukowski, A. (2009). Visualization and analysis of atomistic simulation data with OVITO–the Open Visualization Tool. Model. Simulat. Mater. Sci. Eng. *18*, 015012. https://doi.org/10.1088/0965-0393/18/1/015012.

31. Pirouz, P., Cockayne, D.J.H., Sumida, N., Hirsch, P., and Lang, A.R. (1983). Dissociation of dislocations in diamond. Proc. R. Soc. Lond. A *386*, 241–249.

32. Güler, E., and Güler, M. (2015). Elastic and mechanical properties of cubic diamond under pressure. Chin. J. Phys. *53*, 195–205.

33. Parameswaran, V.R., and Weertman, J. (1971). Dislocation mobility in lead and Pb-In alloy single crystals. Metall. Trans. A *2*, 1233–1243. https://doi.org/10.1007/BF02664257.

34. Ruestes, C.J., Bringa, E.M., Rudd, R.E., Remington, B.A., Remington, T.P., and Meyers, M.A. (2015). Probing the character of ultra-fast dislocations. Sci. Rep. *5*, 16892. https://doi.org/10.1038/srep16892.

35. Hahn, E.N., Zhao, S., Bringa, E.M., and Meyers, M.A. (2016). Supersonic dislocation bursts in silicon. Sci. Rep. *6*, 1–7. https://doi.org/10.1038/srep26977.

36. Zhao, S., Hahn, E.N., Kad, B., Remington, B.A., Wehrenberg, C.E., Bringa, E.M., and Meyers, M.A. (2016). Amorphization and nanocrystallization of silicon under shock compression. Acta Mater. *103*, 519–533. https://doi.org/10.1016/j.actamat.2015.09.022.

37. Orlikowski, D., Correa, A.A., Schwegler, E., Klepeis, J.E., Elert, M., Furnish, M.D., Chau, R., Holmes, N., and Nguyen, J. (2008). A Steinberg-Guinan model for high-pressure carbon: diamond phase. AIP Conf. Proc. *955*, 247. https://doi.org/10.1063/1.2833022.

38. González-Cataldo, F., Godwal, B.K., Driver, K., Jeanloz, R., and Militzer, B. (2021). Model of ramp compression of diamond from ab initio simulations. Phys. Rev. B *104*, 134104. https://doi.org/10.1103/PhysRevB.104.134104.

39. Hicks, D.G., Boehly, T.R., Celliers, P.M., Bradley, D.K., Eggert, J.H., McWilliams, R.S., Jeanloz, R., and Collins, G.W. (2008). High-precision measurements of the diamond Hugoniot in and above the melt region. Phys. Rev. B *78*, 174102. https://doi.org/10.1103/PhysRevB.78.174102.

40. Rowe, P., Deringer, V.L., Gasparotto, P., Csányi, G., and Michaelides, A. (2020). An accurate and transferable machine learning potential for carbon. J. Chem. Phys. *153*, 034702. https://doi.org/10.1063/5.0005084.

41. Willman, J.T., Nguyen-Cong, K., Williams, A.S., Belonoshko, A.B., Moore, S.G., Thompson, A.P., Wood, M.A., and Oleynik, I.I. (2022). Machine learning interatomic potential for simulations of carbon at extreme conditions. Phys. Rev. B *106*, L180101. https://doi.org/10.1103/PhysRevB.106.L180101.

42. Thompson, A.P., Aktulga, H.M., Berger, R., Bolintineanu, D.S., Brown, W.M., Crozier, P.S., in 't Veld, P.J., Kohlmeyer, A., Moore, S.G., Nguyen, T.D., et al. (2022). LAMMPS - a flexible simulation tool for particle-based materials modeling at the atomic, meso, and continuum scales. Comput. Phys. Commun. *271*, 108171. https://doi.org/10.1016/j.cpc.2021.108171.

43. Tersoff, J. (1988). Empirical interatomic potential for silicon with improved elastic properties. Phys. Rev. B *38*, 9902–9905. https://doi.org/10.1103/PhysRevB.38.9902.

44. Nandedkar, A.S., and Narayan, J. (2006). Atomic structure of dislocations in silicon, germanium and diamond *61*, 873–891. https://doi.org/10.1080/01418619008234948.

45. Hu, Z.F., Lv, S.D., Huang, J.F., Zhang, L., Huang, C.T., Li, Y.W., Huang, W.H., Ye, J.P., and Wei, Q. (2018). Anisotropy effects in diamond under nanoindentation. Carbon N Y *38*, 606–611. https://doi.org/10.1016/j.carbon.2018.02.066.